THE JOURNAL OF PHYSICAL CHEMISTRY LETTERS
A JOURNAL OF THE AMERICAN CHEMICAL SOCIETY

pubs.acs.org/JPCL Letter

Anion Photoelectron Spectroscopy and Quantum Chemical Study in ThF^-

Xiao-Gen Xiong,[▽] Changwu Dong,[▽] Hongtao Liu, Zejie Fei,* and Chuangang Ning*

Cite This: https://doi.org/10.1021/acs.jpclett.6c01499 Read Online

ABSTRACT: The photodetachment of ThF^- has been investigated by combining photoelectron spectroscopy with relativistic quantum chemistry calculations. The electron affinity (EA) of ThF is experimentally determined to be 0.680 ± 0.007 eV. We also calculated the adiabatic detachment energy (ADE) and first vertical detachment energy (VDE_1) of the anion to be 0.558 and 0.592 eV at the CCSD(T) level, respectively. The experimentally observed spectroscopic bands were accurately assigned to the relativistic electronic states of ThF with the aid of SO-CASPT2 calculations, and the calculated values are in good agreement with the experimental measurements, with discrepancies within 0.08 eV.

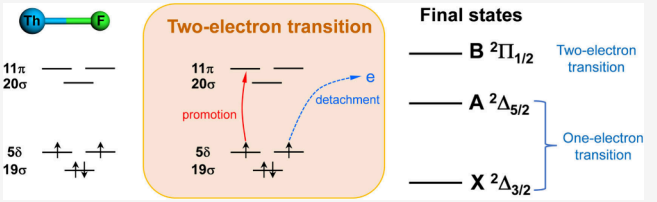

Actinide monofluorides serve as attractive testbeds for relativistic molecular electronic structure methods, as they combine the formal simplicity of diatomic species with dense low-energy manifolds arising from nearly degenerate valence configurations, pronounced spin−orbit coupling, and strong electron correlation effects.[1−5] Such knowledge also has broader relevance to nuclear science and technology, where renewed interest in advanced reactor chemistries, including Generation IV thorium-based molten salt reactors (TMSRs), has spurred research into the physicochemical behavior of actinide halides.[6−10] In thorium fluorides, the close spacing of Th 6*d*-, 7*s*-, and 5*f*-derived valence configurations renders even the lowest-lying electronic states highly sensitive to both relativistic effects and multireference character.[2−5] Gas-phase studies on neutral and cationic ThF have already uncovered this intricate behavior. Laser-induced fluorescence (LIF), resonance-enhanced multiphoton ionization (REMPI), and pulsed field ionization-zero kinetic energy (PFI-ZEKE) spectroscopy have established that neutral ThF possesses an $X\ ^2\Delta_{3/2}$ ground state, with the upper spin−orbit component $X\ ^2\Delta_{5/2}$ located 2575(15) cm^{-1} higher in energy, and have measured an ionization energy of 51581(3) cm^{-1}.[2] Subsequent visible/ultraviolet survey spectroscopy has recorded 345 previously unreported vibronic bands of ThF and refined its spectroscopic characterization over a broad energy range.[11] High-resolution Stark and Zeeman measurements further demonstrated that the ground state is predominantly $^2\Delta_{3/2}$ in character, providing direct information on its electric dipole moment and magnetic *g*-factor.[12] On the cation side, early spectroscopy identified low-lying $^1\Sigma^+$ and $^3\Delta_1$ states separated by only 315.0(5) cm^{-1}, although their ordering could not then be established unambiguously.[2] This issue was subsequently revisited by high-level relativistic theory[4,5] and later resolved experimentally by broadband velocity-modulation spectroscopy, which assigned the electronic ground state of ThF^+ as $X\ ^3\Delta_1$, with a $^1\Sigma^+$ state located about 314 cm^{-1} higher in energy.[13] The spectroscopic interest in ThF^+ is further strengthened by its relevance to searches for the electron's electric dipole moment (eEDM), since ThF^+ has been identified as a promising molecular-ion platform because a heavy atom combined with a low-lying $^3\Delta_1$ state can provide a large internal or effective electric field and favorable coherence properties for precision measurements. More recent precision spectroscopy on the ground state of ThF^+ has refined the hyperfine, dipole-moment, and magnetic *g*-factor constants relevant to ongoing precision-measurement efforts.[14] Earlier high-temperature mass spectrometric studies, combined with later *ab initio* thermochemical investigations, have also established a more comprehensive energetic framework for gaseous thorium fluorides and their ionic species.[15,16]

By contrast, gas-phase studies of ThF^- remain scarce, even though photodetachment from ThF^- offers a direct probe of the low-energy manifolds of the neutral molecule. For a heavy diatomic species such as ThF, where closely spaced spin−orbit components and vibronic levels are expected near the threshold, cryogenic slow-electron velocity-map imaging is especially advantageous because it combines efficient internal cooling with meV-scale energy resolution. As a result, weak near-threshold features that would appear congested or unresolved in

Received: May 8, 2026
Revised: June 3, 2026
Accepted: June 5, 2026

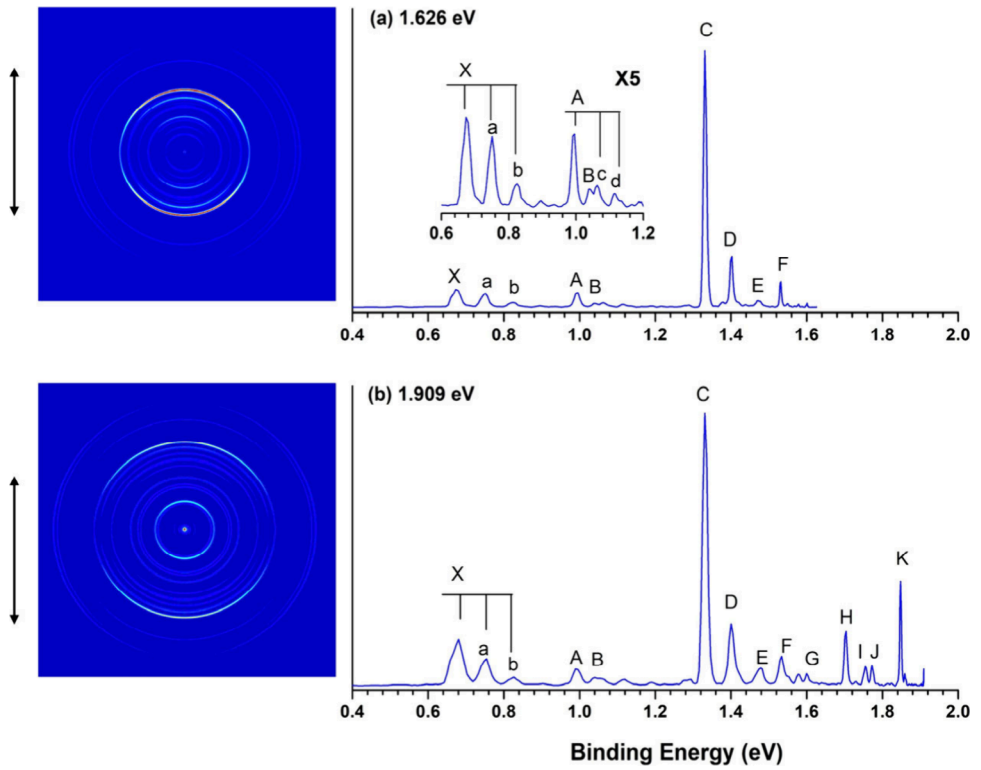

Figure 1. Photoelectron images and spectra of ThF^- at photon energies of (a) 1.626 and (b) 1.909 eV. The vertical lines represent vibrational structures, and the double arrow on the side of the images indicates the laser polarization. The inset in panel (a) shows the peak intensities amplified by a factor of 5.

conventional photoelectron spectra can be separated and assigned with considerably greater confidence. In the present work, we therefore investigate thorium monofluoride from the anion perspective, with particular emphasis on resolving and assigning the low-binding-energy photodetachment transitions of ThF^-. Rather than focusing solely on the overall Th−F bonding picture, we aim to map the low-lying neutral electronic structure with sufficient resolution to identify accessible fine-structure components and vibrational structure. In this way, the present study complements existing spectroscopic work on neutral and cationic ThF and provides a firmer experimental foundation for understanding the low-energy electronic manifold of ThF.

Figure 1 shows the photoelectron spectra of ThF^- at 762.67 and 649.47 nm (photon energies of 1.626 and 1.909 eV) using the SEVI apparatus. Peak X in Figure 1 corresponds to the transition from the anion ground state $^3\sum^-$ to the neutral ground state $^2\Delta_{3/2}$. From the position of peak X, we determine an accurate adiabatic detachment energy (ADE) of 0.680 ± 0.007 eV for ThF^-, which is equal to the electron affinity (EA) of neutral ThF. In Figure 1b, peak X is followed by two features, a and b, at binding energies of 0.754 ± 0.007 and 0.826 ± 0.007 eV, respectively, with a nearly constant spacing of 0.07 eV. We assign these features to the vibrational progression in the neutral ground state, yielding a vibrational frequency of 597 cm^{-1}, in close agreement with the value reported from dispersed fluorescence measurement.[2]

The bands labeled A−K arise from detachment transitions from the anion ground state to electronically excited states of the neutral. Peak A is located at a binding energy of 0.990 ± 0.007 eV, i.e., 0.310 eV above peak X; this feature is assigned to the upper spin−orbit component $^2\Delta_{5/2}$.[2] It is also accompanied by two weak, nearly equally spaced features (c and d), which should correspond to vibrational progression in this excited spin−orbit component, giving a vibrational frequency of 587 cm^{-1}. This value is in good agreement with the 570 cm^{-1} reported from dispersed fluorescence experiments. A weak feature B at 1.042 eV lies on the low-binding energy side of peak c and was not observed in the dispersed fluorescence spectrum. The most intense feature, peak C, is observed at 1.331 ± 0.007 eV; the corresponding photoelectron image in Figure 1 indicates a predominantly parallel transition, consistent with *p*-wave photodetachment. The remaining eight features (D−K) in the binding energy range of 1.400−1.850 eV are observed here for the first time and are assigned with the aid of theoretical calculations. The generally weak intensities of these features suggest that the corresponding transitions to the excited states likely involve significant two-electron character. All the corresponding electron binding energies (EBEs) and the assignment of the labeled peaks are listed in Table 1.

With the purpose of interpreting the experimental spectra and achieving a comprehensive understanding the electronic structures of the studied molecules, we performed substantial amounts of theoretical calculations. The contour plots of the Kohn−Sham molecular orbitals (KS-MOs) of the ThF^- are shown in Figure 2. Our theoretical calculations suggest that the anion has a $^3\sum^-$ ground state with an electron configuration of $(10\pi)^4(19\sigma)^2(5\delta)^2$, and the detachment of one electron from the singly occupied molecular orbital (SOMO) 5δ yields a $^2\Delta$ ground state. The optimized bond lengths and calculated frequencies of the anion and neutral molecule are listed in Table 2. The bond lengths of ThF^- and its corresponding neutral molecule at the CCSD(T) level are 2.080 and 2.021 Å, respectively. The optimized bond length of ThF is consistent

https://doi.org/10.1021/acs.jpclett.6c01499
J. Phys. Chem. Lett. XXXX, XXX, XXX−XXX

Table 1. Experimental EBEs and Theoretical VDEs (in eV) of ThF^-, the Vibrational Frequencies (in cm^{-1}), and the Corresponding Electronic States of ThF[a]

Peak	EBE (exp.)	VDE (theo.)	Freq. (exp.)	Freq. (theo.)	Final SO state
X	0.680	0.680	597	616	$^2\Delta_{3/2}$
A	0.990	1.045	587		$^2\Delta_{5/2}$
B	1.042	1.082			$^2\Pi_{1/2}$
C	1.331	1.343			$^4\sum^-_{1/2}$
D	1.400	1.384			$^2\Pi_{3/2}$
E	1.478	1.427			$^4\Phi_{3/2}$
F	1.533	1.456			$^4\sum^-_{3/2}$
G	1.600	1.615			$^4\Phi_{5/2}$
H	1.704	1.735			$^2\sum^+_{1/2}$
I	1.755	1.812			$^4\Phi_{7/2}$
J	1.772	1.836			$^4\Pi_{1/2}$
K	1.848	1.881			$^4\Pi_{3/2}$

[a]The theoretical VDE_1 was set to the experimental value, and the rest of the VDEs were calculated at the SO-CASPT2 level. The vibrational frequency calculation for neutral ground state was performed at the CCSD(T) level. All calculations were performed using the aug-cc-pwCVQZ for F and cc-pwCVQZ-PP for Th.

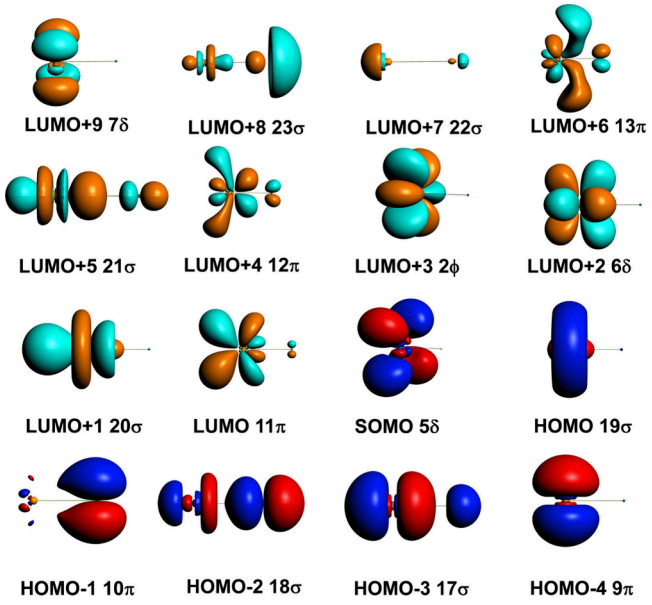

Figure 2. Contour plots of the valence Kohn–Sham MOs (isosurface = 0.05 a.u.) of ThF^- at the PBE level. The electron configuration of ThF^- is $(18\sigma)^2(10\pi)^4(19\sigma)^2(5\delta)^2$.

Table 2. Calculated Bond Lengths and Harmonic Vibrational Harmonic Frequencies of the ThF^- and ThF at Various Levels[a]

	ThF^-		ThF			
	R(Th–F)	Freq.	R(Th–F)	Freq.	ADE	VDE_1
PBE	2.084	530	2.035	595	0.697	0.718
CCSD(T)	2.080	534	2.021	615	0.558	0.592
CASPT2	2.077	-	2.016	-	0.543[b]	0.579

[a]All bond lengths are in Å. All vibrational frequencies are in cm^{-1}, and all energies are in eV. [b]Corrected by ZPEs at the CCSD(T) level.

with previous reports,[17] in which the authors predicted the R(Th–F) to be 2.0254 Å at the scalar relativistic DKH3-CCSD(T) level with the consideration of outer-core correlation. It should also be noted that X2CAMF-CCSD(T) predicted the neutral molecule with a similar Th–F bond length of 2.02937 Å,[12] while the MP2 underestimated the bond length at 1.999 Å.[16] The relatively longer predicted bond lengths at the PBE level may due to the frozen core approximation used in our calculations. After consideration of both the static and dynamic correlations at the CASPT2 level, both the predicted bond lengths of the anion and neutral molecule are slightly shorter than the CCSD(T) values.

The EA of ThF, corresponding to the ADE measured in the PES experiment, was evaluated as the difference between the electronic energies of ThF and ThF^- at their respective equilibrium bond lengths, augmented by a zero-point energy correction. The VDEs were calculated as the energy differences between the anion ground state and the relevant electronic states of the neutral species at the optimized anion geometry. Harmonic vibrational frequency calculations were also performed to obtain the zero-point energies. The ADE and VDE_1 (first VDE) at the PBE, CCSD(T), and CASPT2 levels are also listed in Table 2. At the CCSD(T) level, the ADE and VDE_1 are 0.558 and 0.592 eV, respectively. The calculated vibrational frequencies for ThF at the PBE and CCSD(T) levels are 595 and 615 cm^{-1}, respectively, in comparison with the experimental value of 597 cm^{-1} obtained in the present work.

With the aim of qualitatively understanding the orbital interactions of AOs in ThF^- and spin–orbit splitting of MOs, we draw the energy diagrams of the anion using the molecular orbital energies calculated at the B3LYP[18,19] level with the CCSD(T) optimized geometry, and the diagrams are shown in Figure 3. The reason we choose the B3LYP rather than PBE is because the hybrid functional predicted the correct energy order of 5*f* and 6*d* AOs of Th.[20,21] From Figures 2 and 3, it can be seen

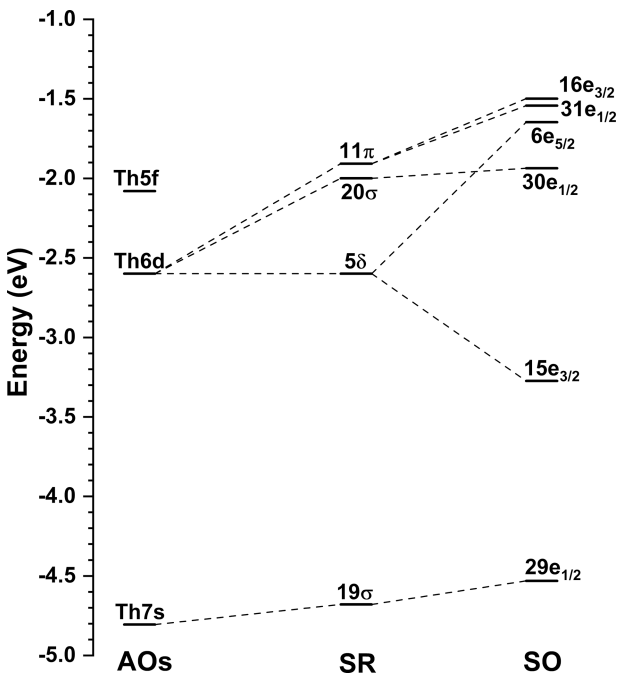

Figure 3. Correlation diagram for the ground state of ThF^- at the scalar and spin–orbit relativistic level. The Kohn–Sham MO energies from ADF/B3LYP single-point calculations were used to draw the diagram. Note the energy levels of ThF^- have been shifted −4.678 eV to offset the electrostatic shift of the negative charge.

https://doi.org/10.1021/acs.jpclett.6c01499
J. Phys. Chem. Lett. XXXX, XXX, XXX–XXX

Table 3. Spin-Free Ground and Low-Lying Excited States of ThF at Its Corresponding Anion Geometry at the CASSCF and CASPT2 Level

State	Main configuration	ΔE(CASSCF) (eV)	ΔE(CASPT2) (eV)	Transition channel
$^2\Delta$	$(19\sigma)^2(5\delta)^1(11\pi)^0$	0.000	0.000	$(5\delta)^{-1}$
$^2\Pi$	$(19\sigma)^2(11\pi)^1(5\delta)^0$	0.414	0.383	$(11\pi)^1(5\delta)^{-2}$
$^4\sum^-$	$(19\sigma)^1(5\delta)^2(11\pi)^0$	0.614	0.597	$(19\sigma)^{-1}$
$^2\sum^+$	$(19\sigma)^2\ (20\sigma)^1(5\delta)^0$	0.829	0.731	$(20\sigma)^1(5\delta)^{-2}$
$^4\Phi$	$(19\sigma)^1(11\pi)^1(5\delta)^1$	0.872	0.880	$(19\sigma)^{-1}(11\pi)^1(5\delta)^{-1}$
$^4\Pi$	$(19\sigma)^1(11\pi)^1(5\delta)^1$	1.064	1.037	$(19\sigma)^{-1}(11\pi)^1(5\delta)^{-1}$
$^2\Gamma$	$(19\sigma)^1(5\delta)^2(11\pi)^0$	1.407	1.276	$(19\sigma)^{-1}(5\delta)^2$[a]
$^4\Delta$	$(19\sigma)^1(20\sigma)^1(5\delta)^1$	1.456	1.363	$(19\sigma)^{-1}(20\sigma)^1(5\delta)^{-1}$

[a]This suggests that the transition involves electronic rearrangement within the 5δ manifold, with one of the 5δ orbitals changing from single to double occupation.

Table 4. Ground and Low-Lying Excited States of ThF at Its Corresponding Anion Geometry at the SO-CASPT2 Level (The Leading Composition and Its Corresponding Electronic Configurations Are Also Included)

Ω	ΔE (eV)	Leading composition	Dominant configurations
3/2	0.000	95.4% $^2\Delta$	$(19\sigma)^2(5\delta)^1$
5/2	0.365	99.9% $^2\Delta$	$(19\sigma)^2(5\delta)^1$
1/2	0.402	82.7% $^2\Pi$ + 13.0% $^2\sum^+$	$(19\sigma)^2(11\pi)^1$, $(19\sigma)^2(20\sigma)^1$
1/2	0.663	68.7% $^4\sum^-$ + 12.6% $^2\sum^+$	$(19\sigma)^1(5\delta)^2$, $(19\sigma)^2(20\sigma)^1$
3/2	0.704	86.6% $^2\Pi$	$(19\sigma)^2(11\pi)^1$
3/2	0.747	76.6% $^4\Phi$ + 15.4% $^4\sum^-$	$(19\sigma)^1(11\pi)^1(5\delta)^1$, $(19\sigma)^1(5\delta)^2$
3/2	0.776	75.1% $^4\sum^-$ + 15.0% $^4\Phi$	$(19\sigma)^1(5\delta)^2$, $(19\sigma)^1(11\pi)^1(5\delta)^1$
5/2	0.935	90.4% $^4\Phi$ + 7.1% $^4\Delta$	$(19\sigma)^1(11\pi)^1(5\delta)^1$, $(19\sigma)^1(20\sigma)^1(5\delta)^1$
1/2	1.055	62.2% $^2\sum^+$ + 11.2% $^4\sum^-$ + 13.5% $^4\Pi$	$(19\sigma)^2(20\sigma)^1$, $(19\sigma)^1(5\delta)^2$, $(19\sigma)^1(11\pi)^1(5\delta)^1$
7/2	1.132	84.9% $^4\Phi$	$(19\sigma)^1(11\pi)^1(5\delta)^1$
1/2	1.156	65.7% $^4\Pi$ + 14.6% $^4\Delta$ + 9.6% $^2\sum^+$	$(19\sigma)^1(11\pi)^1(5\delta)^1$, $(19\sigma)^1(20\sigma)^1(5\delta)^1$, $(19\sigma)^2(20\sigma)^1$
3/2	1.201	73.1% $^4\Pi$ + 18.0% $^4\Delta$	$(19\sigma)^1(11\pi)^1(5\delta)^1$, $(19\sigma)^1(20\sigma)^1(5\delta)^1$
1/2	1.216	79.9% $^4\Pi$ + 11.3% $^4\sum^-$	$(19\sigma)^1(11\pi)^1(5\delta)^1$, $(19\sigma)^1(5\delta)^2$
5/2	1.248	86.9% $^4\Pi$ + 9.2% $^4\Delta$	$(19\sigma)^1(11\pi)^1(5\delta)^1$, $(19\sigma)^1(20\sigma)^1(5\delta)^1$
9/2	1.318	72.1% $^4\Phi$ + 23.4% $^2\Gamma$	$(19\sigma)^1(11\pi)^1(5\delta)^1$, $(19\sigma)^1(5\delta)^2$
7/2	1.475	86.5% $^2\Gamma$ + 9.4% $^4\Delta$	$(19\sigma)^1(5\delta)^2$, $(19\sigma)^1(20\sigma)^1(5\delta)^1$
1/2	1.493	61.7% $^4\Delta$ + 25.2% $^4\Pi$	$(19\sigma)^1(20\sigma)^1(5\delta)^1$, $(19\sigma)^1(11\pi)^1(5\delta)^1$
9/2	1.548	71.6% $^2\Gamma$ + 26.9% $^4\Phi$	$(19\sigma)^1(5\delta)^2$, $(19\sigma)^1(11\pi)^1(5\delta)^1$
3/2	1.626	76.9% $^4\Delta$ + 20.2% $^4\Pi$	$(19\sigma)^1(20\sigma)^1(5\delta)^1$, $(19\sigma)^1(11\pi)^1(5\delta)^1$
5/2	1.721	83.7% $^4\Delta$ + 11.7% $^4\Pi$	$(19\sigma)^1(20\sigma)^1(5\delta)^1$, $(19\sigma)^1(11\pi)^1(5\delta)^1$
7/2	1.777	93.6% $^4\Delta$	$(19\sigma)^1(20\sigma)^1(5\delta)^1$

that in the anion, the 5δ degenerate orbitals are dominated by the Th $6d_\delta$ atomic orbitals and therefore exhibit a pronounced spin−orbit splitting. The highly occupied molecular orbital (HOMO) 19σ has the main contribution from the linear combination Th $7s$ and $6d_\sigma$ atomic orbitals. All of these three MOs can be categorized as nonbonding orbitals. The $2p_\sigma$ AO of F interacts with the Th $7s$ and $6d_\sigma$ and forms the bonding orbital 18σ, while the 10π MOs mainly stem from the $2p_\pi$ AOs of fluorine. Although the PBE and B3LYP predicted the reverse order of the 11π and 20σ MOs, all of these three orbitals are dominated by the Th $6d$ AOs but with minor contributions of Th $5f$ AOs, and the 11π also shows non-negligible spin−orbit splitting.

In an attempt to accurately calculate the energies of the electronic states incorporating the spin−orbit splitting to assign the observed band in the experimental spectra, we performed the SO-CASPT2 calculations of ThF at its corresponding anion geometry optimized at the CCSD(T) level. The active spaces used in our calculations include 19σ, 5δ, 11π, 20σ, 6δ, 2ϕ, 12π, 21σ, 13π, and 22σ MOs, as shown in Figure 2. Table 3 lists the spin-free eigenstates included in the calculations, comprising the ground state and the selected low-lying excited states. The main configuration of each state and the calculated relative energies at both CASSCF and CASPT2 levels are also presented. At the scalar relativistic level, the first excited state of the neutral molecule is $^2\Pi$ with a dominant configuration of $(10\pi)^4(19\sigma)^2(11\pi)^1$. This assignment indicates that the corresponding photodetachment channel cannot be described as a simple one-electron process, but instead involves substantial electronic rearrangement. The second excited state is $^4\sum^-$ with a main configuration of $(19\sigma)^1(5\delta)^2$. These two lowest-lying excited states are 0.383 and 0.597 eV higher than the ground states, respectively. The remaining excited states listed in Table 3 can be understood in terms of changes in orbital occupation relative to the ground-state configuration. Their formation, however, cannot be described as simple direct one-electron detachment, since substantial electronic rearrangement is involved. The transition patterns indicate that, except for the $^2\Delta$ and $^4\sum^-$ final states, the other channels possess appreciable rearrangement character. This interpretation accounts for the spectral profile in Figure 1b, where the other excited-state peaks are significantly weaker than peak C.

After perturbative treatment of the spin−orbit coupling, the resulting SO relativistic states are detailed listed in Table 4. The

https://doi.org/10.1021/acs.jpclett.6c01499
J. Phys. Chem. Lett. XXXX, XXX, XXX−XXX

theoretical VDEs derived from SO-CASPT2 calculations, as presented in Table 1, are in good agreement with the experimental data. Our SO-CASPT2 calculations indicate a spin−orbit splitting energy of 0.365 eV for the ground state of ThF, yielding two relativistic states with Ω equal to 3/2 and 5/2, respectively, and the observed experimental peaks X and A with a splitting energy of 0.310 eV can be assigned to these two states. The band B with low intensity can be assigned to a state with Ω = 1/2, and similar as in ThO,[20] this detachment channel can be viewed as a two-electron transition, in which one 5δ electron is detached and the other is excited to 11π or 20σ. The peak C with the highest intensity in our experiment is also assigned to a state with Ω = 1/2, and this band can be viewed as the detachment channel from 19σ MO. The high intensity may due to the direct one-electron detachment process and diffuse character of the Th 7*s* AO, which therefore has a large cross-section with the incident photon. The band D can also be viewed as the same two-electron transition as band B but with a large Ω value and hence a relatively higher intensity. It should be noted that the present work predicts a reversed energetic ordering for the third and fourth excited state compared with Irikura's reports, and his reported excitation energies also deviate slightly from those obtained in this study.[16]

We assign bands E, G, and I with binding energies of 1.478, 1.600, and 1.755 eV to relativistic states $^4\Phi_{3/2}$, $^4\Phi_{5/2}$, and $^4\Phi_{7/2}$, and we can understand these three channels as the detachment of one electron from 5δ MO and one electron excited from 19σ to 11π, which are also two-electron transition processes. Band F, similar to band C, can be assigned to electron detachment from the HOMO (19σ), rather than from the SOMO. The energy separation between bands C and F may be attributed to the spin−spin coupling within the $^4\Sigma^-$ state, together with additional second-order spin−orbit contributions. The peak H is assigned to a relativistic state $^2\sum^+_{1/2}$, and this state has the main compositions of scalar relativistic states $^2\sum^+$, $^4\sum^-$, $^4\Pi$, etc. The J and K bands correspond to the two relativistic states $^4\Pi_{1/2}$ and $^4\Pi_{3/2}$, which can also be described as a two-electron transition.

In summary, the high-resolution photoelectron spectrum of ThF^- was measured by cryo-SEVI. The electron affinity of ThF was determined to be 0.680 ± 0.007 eV, and the experimentally measured excited-state energies are in excellent agreement with the SO-CASPT2 calculations. In contrast, scalar-relativistic spin-free CASPT2 underestimates the ADE by 0.14 eV, underscoring the importance of spin−orbit coupling in thorium-containing species with closely spaced low-lying valence configurations, as well as the value of accurate experimental benchmarks for key thermodynamic quantities. The complex spectral features can be consistently assigned with the aid of spin−orbit-coupled calculations, and the computational results further suggest that the generally weak intensities of most bands originate from the significant two-electron character of the corresponding excited-state transitions.

EXPERIMENTAL AND COMPUTATIONAL METHODS

The cryogenically cooled slow-electron velocity-map imaging (cryo-SEVI) apparatus[22,23] was employed in this work and has been widely used for photoelectron spectroscopy studies of atomic and molecular clusters.[24−28] The ThF^- was generated by laser ablation of a thorium metal disk in the presence of NF_3 gas. The resulting anions were trapped in an octupole radio frequency (RF) ion trap and cooled by collisions with a buffer gas mixture of 20% H_2 and 80% He. The ion trap was mounted on the second stage of a liquid helium refrigerator with a tunable temperature ranging from 5 to 300 K.[29,30] The cooled anions were then extracted by pulsed potentials applied to the trap end-caps and analyzed with a Wiley−McLaren type time-of-flight (TOF) mass spectrometer.[31,32] Mass-selected ThF^- anions (m/z = 251) were focused into the interaction region of a velocity-map imaging (VMI) spectrometer and photodetached by irradiation with a tunable laser. The photoelectrons were projected onto a 2D position-sensitive detector using a set of electrostatic lenses and recorded by a charge-coupled device (CCD) camera. Owing to the cylindrical symmetry of the photoelectron distribution, the three-dimensional photoelectron distribution was reconstructed from the projected two-dimensional image via the maximum entropy velocity Legendre reconstruction (MEVELER) method, from which the electron kinetic energy distribution was obtained. In addition, the photoelectron spectrum yields the electron affinity (EA) and vibrational frequencies of the corresponding neutral species, as well as the ADE and vertical detachment energy (VDE) of the anion.

Both density functional theory (DFT) and wave function theory (WFT) calculations were performed to study ThF^- and its corresponding neutral molecule. The PBE[33] exchange-correlation functional implemented in the Amsterdam Density Functional (ADF 2016.01)[34] was used in our DFT calculations, and the Slater basis sets with the quality of triple-ζ plus two polarization functions (TZ2P) were used, in which the frozen core approximation was applied to the inner shells [$1s^2$−$5d^{10}$] for Th and [$1s^2$] for F. In order to predict more accurate geometries and vibrational frequencies, we also carried out the electron correlation calculations at the coupled-cluster singles and doubles plus perturbative triples (CCSD(T))[35,36] and complete-active space second-order perturbation theory (CASPT2)[37,38] levels using Molpro2021.3.[39] In our coupled-cluster and multireference calculations, the Stuttgart energy-consistent relativistic pseudopotentials ECP60MDF[40] and the corresponding augmented valence quadruple-ζ basis sets with weighted core functions cc-pwCVQZ-PP were used for Th,[41,42] and the all-electron basis sets aug-cc-pwCVQZ were used for F.[43,44] All electrons, i.e., 39 electrons in ThF and 40 electrons in ThF^-, are correlated in our WFT calculations.

For the purpose of accurately assigning the spectral peaks of the experimental PES, we calculated the energies of the SO relativistic states of the neutral molecule at its corresponding anion geometry using the SO-CASPT2 approach, which has been proven to be able to reliably predict the low-lying excited-state energies of thorium-containing molecules.[20,21] Briefly speaking, in this approach, the spin−orbit effects were considered perturbatively through the SO potentials for thorium and the Breit−Pauli (BP) operator for fluorine, and state energies were calculated by diagonalizing the Hamiltonian including the spin−orbit operator in a basis of spin-free complete active space self-consistent field (CASSCF)[45−47] eigenstates. So as to thoroughly consider both the static and dynamic correlation to the energies of the studied scalar-relativistic states, the state-specific CASPT2 calculations using the same state-average CASSCF wave functions in SO calculations were performed for the selected spin-free states, and the predicted CASPT2 energies were utilized to replace the diagonal matrix elements of the SA-CASSCF wave functions. The level shift technique with 0.3 a.u. was used in our CASPT2 calculations to avoid intruder states and improve the convergence, and the empirical ionization potential-electron affinity (IPEA) correction applied to zeroth-order Hamiltonian[48] with a shift value of 0.2 a.u. was also adopted to correct the systematic error of the overestimation of the correlation energy for open-shell molecules. In all our multireference calculations, the active space includes 3 electrons and 16 orbitals (dominated by 5*f*, 6*d*, 7*s*, and 7*p* atomic orbitals of thorium), thus yielding a CAS(3e, 16o) active space.

ASSOCIATED CONTENT

Data Availability Statement

All data generated in this study are provided in the article. Other experimental and theoretical data that support the findings of this study are available from the corresponding authors upon request.

https://doi.org/10.1021/acs.jpclett.6c01499
J. Phys. Chem. Lett. XXXX, XXX, XXX−XXX

AUTHOR INFORMATION

Corresponding Authors

Zejie Fei − *Key Laboratory of Interfacial Physics and Technology, Shanghai Institute of Applied Physics, Chinese Academy of Sciences, Shanghai 201800, P. R. China*; Email: feizejie@sinap.ac.cn

Chuangang Ning − *Department of Physics, State Key Laboratory of Low Dimensional Quantum Physics, Frontier Science Center for Quantum Information, Tsinghua University, Beijing 100084, P. R. China*; orcid.org/0000-0002-3158-1253; Email: ningcg@tsinghua.edu.cn

Authors

Xiao-Gen Xiong − *Sino-French Institute of Nuclear Engineering and Technology, Sun Yat-sen University, Zhuhai 519082, P. R. China; CNPRI-SYSU Joint Research Center for Coolant Chemistry of Nuclear Reactor, Zhuhai 519082, P. R. China*; orcid.org/0000-0002-3230-9657

Changwu Dong − *Key Laboratory of Interfacial Physics and Technology, Shanghai Institute of Applied Physics, Chinese Academy of Sciences, Shanghai 201800, P. R. China*; orcid.org/0000-0002-5642-5310

Hongtao Liu − *Key Laboratory of Interfacial Physics and Technology, Shanghai Institute of Applied Physics, Chinese Academy of Sciences, Shanghai 201800, P. R. China*; orcid.org/0000-0001-6450-2585

Complete contact information is available at: https://pubs.acs.org/10.1021/acs.jpclett.6c01499

Author Contributions

[▽]X.-G.X. and C.D. contributed equally to this work.

Notes

The authors declare no competing financial interest.

ACKNOWLEDGMENTS

This work was supported by the National Natural Science Foundation of China (Grant No. 22273121, 22273065, 12374244, and 12341401) and the Youth Innovation Promotion Association, Chinese Academy of Science (No. 2021255). The calculations were performed at in-house workstations.

REFERENCES

(1) Meyer, E. R.; Bohn, J. L. Prospects for an electron electric-dipole moment search in metastable ThO and ThF^+. *Phys. Rev. A* **2008**, *78* (1), No. 010502.

(2) Barker, B. J.; Antonov, I. O.; Heaven, M. C.; Peterson, K. A. Spectroscopic investigations of ThF and ThF^+. *J. Chem. Phys.* **2012**, *136* (10), 104305 DOI: 10.1063/1.3691301.

(3) Heaven, M. C.; Barker, B. J.; Antonov, I. O. Spectroscopy and Structure of the Simplest Actinide Bonds. *J. Phys. Chem. A* **2014**, *118* (46), 10867−10881.

(4) Denis, M.; Nørby, M. S.; Jensen, H. J. A.; Gomes, A. S. P.; Nayak, M. K.; Knecht, S.; Fleig, T. Theoretical study on ThF^+, a prospective system in search of time-reversal violation. *New J. Phys.* **2015**, *17* (4), No. 043005.

(5) Skripnikov, L. V.; Titov, A. V. Theoretical study of ThF^+ in the search for *T, P*-violation effects: Effective state of a Th atom in ThF^+ and ThO compounds. *Phys. Rev. A* **2015**, *91* (4), No. 042504.

(6) Nuttin, A.; Heuer, D.; Billebaud, A.; Brissot, R.; Le Brun, C.; Liatard, E.; Loiseaux, J. M.; Mathieu, L.; Meplan, O.; Merle-Lucotte, E.; et al. Potential of thorium molten salt reactorsdetailed calculations and concept evolution with a view to large scale energy production. *Prog. Nucl. Energy* **2005**, *46* (1), 77−99.

(7) György, H.; Czifrus, S. The utilization of thorium in Generation IV reactors. *Prog. Nucl. Energy* **2016**, *93*, 306−317.

(8) Gehin, J. C.; Powers, J. J. Liquid Fuel Molten Salt Reactors for Thorium Utilization. *Nucl. Technol.* **2016**, *194* (2), 152−161.

(9) Zhang, D.; Liu, L.; Liu, M.; Xu, R.; Gong, C.; Zhang, J.; Wang, C.; Qiu, S.; Su, G. Review of conceptual design and fundamental research of molten salt reactors in China. *Int. J. Energy Res.* **2018**, *42* (5), 1834−1848.

(10) Zhang, Y.-P.; Ma, Y.-W.; Wu, J.-H.; Chen, J.-G.; Cai, X.-Z. Preliminary analysis of fuel cycle performance for a small modular heavy water-moderated thorium molten salt reactor. *Nucl. Sci. Technol.* **2020**, *31* (11), 108.

(11) Zhou, Y.; Ng, K. B.; Cheng, L.; Gresh, D. N.; Field, R. W.; Ye, J.; Cornell, E. A. Visible and ultraviolet laser spectroscopy of ThF. *J. Mol. Spectrosc.* **2019**, *358*, 1−16.

(12) Nguyen, D.-T.; Steimle, T.; Linton, C.; Cheng, L. Optical Stark and Zeeman Spectroscopy of Thorium Fluoride (ThF) and Thorium Chloride (ThCl). *J. Phys. Chem. A* **2019**, *123* (7), 1423−1433.

(13) Gresh, D. N.; Cossel, K. C.; Zhou, Y.; Ye, J.; Cornell, E. A. Broadband velocity modulation spectroscopy of ThF^+ for use in a measurement of the electron electric dipole moment. *J. Mol. Spectrosc.* **2016**, *319*, 1−9.

(14) Ng, K. B.; Zhou, Y.; Cheng, L.; Schlossberger, N.; Park, S. Y.; Roussy, T. S.; Caldwell, L.; Shagam, Y.; Vigil, A. J.; Cornell, E. A.; et al. Spectroscopy on the electron-electric-dipole-moment-sensitive states of ThF^+. *Phys. Rev. A* **2022**, *105* (2), No. 022823.

(15) Lau, K. H.; Brittain, R. D.; Hildenbrand, D. L. High temperature thermodynamic studies of some gaseous thorium fluorides. *J. Chem. Phys.* **1989**, *90* (2), 1158−1164.

(16) Irikura, K. K. Gas-Phase Energetics of Thorium Fluorides and Their Ions. *J. Phys. Chem. A* **2013**, *117* (6), 1276−1282.

(17) Kawagoe, T. T.; Merriles, D. M.; Morse, M. D.; Peterson, K. A. Bond Dissociation Energies and Electronic Calculations on the Actinide Halides ThX and UX (X = Cl, Br, I). *J. Phys. Chem. A* **2025**, *129* (34), 7842−7852.

(18) Becke, A. D. Density-functional thermochemistry. III. The role of exact exchange. *J. Chem. Phys.* **1993**, *98* (7), 5648−5652.

(19) Stephens, P. J.; Devlin, F. J.; Chabalowski, C. F.; Frisch, M. J. Ab Initio Calculation of Vibrational Absorption and Circular Dichroism Spectra Using Density Functional Force Fields. *J. Phys. Chem.* **1994**, *98* (45), 11623−11627.

(20) Li, Y.; Zou, J.; Xiong, X.-G.; Su, J.; Xie, H.; Fei, Z.; Tang, Z.; Liu, H. Probing Chemical Bonding and Electronic Structures in ThO^- by Anion Photoelectron Imaging and Theoretical Calculations. *J. Phys. Chem. A* **2017**, *121* (10), 2108−2113.

(21) Fei, Z.; Wang, J.-Q.; Tang, R.; Lu, Y.; Han, C.; Wang, Y.; Hong, J.; Dong, C.; Hu, H.-S.; Xiong, X.-G.; et al. The unusual quadruple bonding of nitrogen in ThN. *Nat. Commun.* **2023**, *14* (1), 7677.

(22) Tang, R.; Si, R.; Fei, Z.; Fu, X.; Lu, Y.; Brage, T.; Liu, H.; Chen, C.; Ning, C. Candidate for Laser Cooling of a Negative Ion: High-Resolution Photoelectron Imaging of Th^-. *Phys. Rev. Lett.* **2019**, *123* (20), 203002 DOI: 10.1103/PhysRevLett.123.203002.

(23) Tang, R.; Si, R.; Fei, Z.; Fu, X.; Lu, Y.; Brage, T.; Liu, H.; Chen, C.; Ning, C. Observation of Electric-Dipole Transitions in the Laser-Cooling Candidate Th. *Phys. Rev. A* **2021**, *103* (4), No. 042817.

(24) Tang, R.; Lu, Y.; Liu, H.; Ning, C. Electron affinity of uranium and bound states of opposite parity in its anion. *Phys. Rev. A* **2021**, *103*, No. L050801.

(25) Weichman, M. L.; Neumark, D. M. Slow Photoelectron Velocity-Map Imaging of Cryogenically Cooled Anions. *Annu. Rev. Phys. Chem.* **2018**, *69* (1), 101−124.

(26) Tang, R.; Fu, X.; Ning, C. Accurate electron affinity of Ti and fine structures of its anions. *J. Chem. Phys.* **2018**, *149*, No. 134304.

(27) Wang, L. S.; Ding, C. F.; Wang, X. B.; Barlow, S. E. Photodetachment photoelectron spectroscopy of multiply charged anions using electrospray ionization. *Rev. Sci. Instrum.* **1999**, *70* (4), 1957−1966.

(28) Luo, Z.; Chen, X.; Li, J.; Ning, C. Precision measurement of the electron affinity of niobium. *Phys. Rev. A* **2016**, *93* (2), No. 020501.
(29) Wang, X. B.; Wang, L. S. Development of a low-temperature photoelectron spectroscopy instrument using an electrospray ion source and a cryogenically controlled ion trap. *Rev. Sci. Instrum.* **2008**, *79* (7), 2008.
(30) Hock, C.; Kim, J. B.; Weichman, M. L.; Yacovitch, T. I.; Neumark, D. M. Slow photoelectron velocity-map imaging spectroscopy of cold negative ions. *J. Chem. Phys.* **2012**, *137* (24), No. 244201.
(31) Wiley, W. C.; Mclaren, I. H. Time-of-Flight Mass Spectrometer with Improved Resolution. *Rev. Sci. Instrum.* **1955**, *26* (12), 1150.
(32) León, I.; Yang, Z.; Liu, H.-T.; Wang, L.-S. The design and construction of a high-resolution velocity-map imaging apparatus for photoelectron spectroscopy studies of size-selected clusters. *Rev. Sci. Instrum.* **2014**, *85* (8), 083106.
(33) Perdew, J. P.; Burke, K.; Ernzerhof, M. Generalized Gradient Approximation Made Simple. *Phys. Rev. Lett.* **1996**, *77* (18), 3865−3868.
(34) *ADF 2016.01*; SCM, Theoretical Chemistry, Vrije Universiteit, Amsterdam, The Netherlands. http://www.scm.com.
(35) Scuseria, G. E.; Janssen, C. L.; Schaefer, H. F. I. An efficient reformulation of the closed-shell coupled cluster single and double excitation (CCSD) equations. *J. Chem. Phys.* **1988**, *89* (12), 7382−7387.
(36) Watts, J. D.; Gauss, J.; Bartlett, R. J. Coupled-cluster methods with noniterative triple excitations for restricted open-shell Hartree−Fock and other general single determinant reference functions. Energies and analytical gradients. *J. Chem. Phys.* **1993**, *98* (11), 8718−8733.
(37) Andersson, K.; Malmqvist, P. Å.; Roos, B. O. Second-order perturbation theory with a complete active space self-consistent field reference function. *J. Chem. Phys.* **1992**, *96* (2), 1218−1226.
(38) Celani, P.; Werner, H.-J. Multireference perturbation theory for large restricted and selected active space reference wave functions. *J. Chem. Phys.* **2000**, *112* (13), 5546−5557.
(39) Werner, H.-J.; Knowles, P. J.; et al. *MOLPRO 2021.3, a package of ab initio programs*. https://www.molpro.net.
(40) Weigand, A.; Cao, X.; Hangele, T.; Dolg, M. Relativistic Small-Core Pseudopotentials for Actinium, Thorium, and Protactinium. *J. Phys. Chem. A* **2014**, *118* (13), 2519−2530.
(41) Peterson, K. A. Correlation consistent basis sets for actinides. I. The Th and U atoms. *J. Chem. Phys.* **2015**, *142* (7), 074105.
(42) Vasiliu, M.; Peterson, K. A.; Gibson, J. K.; Dixon, D. A. Reliable Potential Energy Surfaces for the Reactions of H_2O with ThO_2, PaO_2^+, UO_2^{2+}, and UO_2^+. *J. Phys. Chem. A* **2015**, *119* (46), 11422−11431.
(43) Dunning, T. H., Jr. Gaussian basis sets for use in correlated molecular calculations. I. The atoms boron through neon and hydrogen. *J. Chem. Phys.* **1989**, *90* (2), 1007−1023.
(44) Kendall, R. A.; Dunning, T. H. Jr.; Harrison, R. J. Electron affinities of the first-row atoms revisited. Systematic basis sets and wave functions. *J. Chem. Phys.* **1992**, *96* (9), 6796−6806.
(45) Knowles, P. J.; Werner, H.-J. An efficient second-order MC SCF method for long configuration expansions. *Chem. Phys. Lett.* **1985**, *115* (3), 259−267.
(46) Werner, H. J.; Knowles, P. J. A second order multiconfiguration SCF procedure with optimum convergence. *J. Chem. Phys.* **1985**, *82* (11), 5053−5063.
(47) Kreplin, D. A.; Knowles, P. J.; Werner, H.-J. Second-order MCSCF optimization revisited. I. Improved algorithms for fast and robust second-order CASSCF convergence. *J. Chem. Phys.* **2019**, *150* (19), 194106.
(48) Ghigo, G.; Roos, B. O.; Malmqvist, P.-Å. A modified definition of the zeroth-order Hamiltonian in multiconfigurational perturbation theory (CASPT2). *Chem. Phys. Lett.* **2004**, *396* (1), 142−149.

https://doi.org/10.1021/acs.jpclett.6c01499
J. Phys. Chem. Lett. XXXX, XXX, XXX−XXX